Contents lists available at ScienceDirect

Applied Catalysis B: Environmental

Ceria-based electrolytes prepared by solution combustion synthesis: The role of fuel on the materials properties

C. Aliotta [a],*, L.F. Liotta [b], V. La Parola [b], A. Martorana [a], E.N.S Muccillo [c], R. Muccillo [c], F. Deganello [b]

[a] Università degli Studi di Palermo, Dipartimento di Fisica e Chimica, edificio 17, viale delle Scienze, I-90128 Palermo, Italy
[b] Istituto per lo Studio dei Materiali Nanostrutturati, Consiglio Nazionale delle Ricerche, via U. La Malfa, I-90146 Palermo, Italy
[c] Centro de Ciência e Tecnologia de Materiais, Instituto de Pesquisas Energéticas e Nucleares, Cidade Universitària, S. Paulo, SP, Brazil

ARTICLE INFO

ABSTRACT

$Ce_{0.8}Sm_{0.2}O_{2-x}$ powders were synthesized by solution combustion synthesis using citric acid, cellulose and sucrose as single, or intimately mixed, fuels. The powders were characterized by X-ray diffraction, transmission electron microscopy, X-ray photoelectron spectroscopy, N_2 sorption at $-196\,°C$, H_2-temperature programmed reduction and thermogravimetric analyses. Textural properties of the powders were shaped by the peculiar employed fuel. The study of reducibility revealed that oxygen vacancies formation is mainly influenced by both parameters, specific surface area and total pore volume. The different tendency toward reduction played a key role in sintering under reducing atmosphere (4% H_2/Ar), and $Ce_{0.8}Sm_{0.2}O_{2-x}$ prepared with sucrose showed, at scanning electron microscopy images, the highest average grain size. Impedance spectroscopy experiments in air disclosed different grain boundary resistances on the basis of synthesis fuel employed and, in particular, $Ce_{0.8}Sm_{0.2}O_{2-x}$ prepared with sucrose exhibited the best electrical performance. Solution combustion synthesis thereby was able to tailor the morphological and reduction properties of $Ce_{0.8}Sm_{0.2}O_{2-x}$ powders affecting even the microstructure of sintered pellet.

1. Introduction

Nowadays, the research on electrolytes for solid oxide fuel cells (SOFCs) is voted to the development of materials able to enhance the electrical efficiency in the intermediate temperature range (IT-), *ca.* 500–800 °C. Due to the high ionic conductivity below 900 °C, lanthanides doped cerium oxides ($Ce_{1-y}Ln_yO_{2-x}$) represent the most reliable candidates for a large scale technological development of SOFC devices [1–4]. Doping of CeO_2 with a trivalent rare earth element introduces, for charge compensation, an opportune amount of oxygen vacancies ($V_O^{••}$) that allow charge transport by drift through oxide matrix. However, at the dopant concentration of about 10–20%, necessary to achieve a suitable ionic conductivity, the formation of stable complexes $Ln - V_O^{••}$ might block the oxygen vacancies and hinder the ionic transport. For dopant content besides 20 at.% the ionic conductivity is strongly blocked. According to the literature, samarium – just followed by gadolinium – is the most promising dopant, not only due to its proper ionic radius,

but also to a lower tendency to form $Sm - V_O^{••}$ complexes [3,5,6]. However, the accurate selection of type and content of dopant is not sufficient to ensure suitable electrical performance, because at the grain boundaries accumulation of $V_O^{••}$ and Sm(III) might hinder the conductivity. As the grain boundary resistance represents the limiting factor for the overall electrical performance, the fine texture of the electrolyte material is of paramount importance [7–10]. In this respect, firstly a full density material (90–97%) is required for enhancing the ionic transport and, secondly, alio-dopant and impurities segregation to the grain boundaries must be minimized. Actually, special attention has been paid to sintering mechanism of doped ceria and it is, on the whole, established that grain growth is promoted by surface and grain boundary diffusions at the early stages of sintering, whereas at high temperature lattice diffusion mechanism activates densification and exclusion of pores. However, segregation phenomena to the grain boundaries interfere with diffusion process limiting the coarsening of particles [11–13]. Consequently, suitable particle size and porosity of powders used for membrane fabrication are pivotal for the microstructure and density of the final material. To design doped ceria as electrolyte it is mandatory to define peculiar sintering procedures and synthesis method for shaping the starting powders and achieving effec-

tive electrolytic membranes. For instance, Esposito *et al.* referred that employing nanostructured Sm- or Gd-doped (20 at.%) ceria, as starting powders for fast firing sintering, allows to reduce the grain boundary contribution to the to total conductivity. Thanks to high surface energy of small sized particles and to short sintering time, full density materials have been obtained with low grain growth and limited segregation phenomena [11]. Esposito et al. successively explored the sintering of $Ce_{0.9}Gd_{0.1}O_{2-x}$, (CGO), both with high and low specific surface area, in 9% H_2/N_2 with the purpose of forming an opportune amount of oxygen vacancies on the surface of particles for favouring the densification. Authors noted that high densification was reached at lower temperatures compared to conventional temperatures reached in air. Furthermore electrical conductivity of CGO sintered under 9% H_2/N_2 was competitive with the value extrapolated for CGO conventionally sintered [12]. More recently, Ni *et al.* investigated the effects of slurry-based techniques for shaping the porosity of CGO powders. They verified that pore sizes affect grain growth and, in particular, small pores were determinant for densification at the initial stage of sintering, whereas large pores influenced the sintering process at high temperature [13]. Several papers dealt with methods able to produce porous material with controlled grain size, in most of them the use of auxiliary substances is reported [14–16]. On the other hand, the use of additives renders more cumbersome the overall membrane fabrication procedure and may have a negative impact on the total conductivity. Almost always, it is possible to bypass these aided methods selecting a suitable synthesis method: in this light, solution combustion synthesis (SCS) represents a flexible method to produce, by single step, nanostructured and ultra-fine powders with suitable microstructural properties [17–23]. According to the method, the synthesis fuel has the triple role of: (i) propellant, (ii) complexing agent, (iii) microstructural template. Playing with the fuel, it is possible to modulate the microstructure of powder and to create an adequate porous network which represents a fundamental starting point for the densification process [24–27].

The present work aims to evaluate the effect of SCS on morphological properties of $Ce_{0.8}Sm_{0.2}O_{2-x}$ powders and to assess the impact of sintering under 4% H_2/Ar on the electrical properties of the final products. In this respect, three different fuel of synthesis were selected: citric acid, cellulose-citric acid and sucrose. The powders were characterized by XRD, XPS, TEM and N_2 adsorption at −196 °C. Moreover, H_2-TPR and TGA analyses were carried out in order to evaluate the presence of surface oxygen vacancies and as well the capacity of powders to create oxygen vacancies at high temperature under reducing atmosphere with a view to correlate reduction features with microstructure after sintering under hydrogen atmosphere. Special efforts were brought in relating powder and sintered material microstructure with electrical performance.

2. Experimental

2.1. Materials preparation

$Ce_{0.8}Sm_{0.2}O_{2-x}$ powders were prepared by solution combustion synthesis using $Ce(NO_3)_3 \cdot 6H_2O$ (99.99% Sigma-Aldrich) and $Sm(NO_3)_3 \cdot 6H_2O$ (99.99% Sigma-Aldrich) as metal precursors and as combustion fuel mixtures: 1) citric acid ($C_6H_5O_7$ anhydrous, ≥99.5% Sigma-Aldrich) with ammonia (28 vol.% NH_3 in H_2O, ≥99,99% Sigma-Aldrich); 2) cellulose (powder with degree of substitution zero, DS-0, for thin layer chromatography, Fluka Analytical) and citric acid in the 2:1 molar ratio; 3) sucrose (Eridania Italia Spa ©). According to propellants chemistry [28], the combustion reactions were carried out in stoichiometric condition (Φ = reducers-to-oxidizers molar ratio = 1) with a fuel-to-metal

cations molar ratio set to 2. To achieve this purpose, a proper amount of ammonium nitrate (NH_4NO_3, ≥99,0% Sigma-Aldrich) was added to reaction mixtures as oxidant regulator for fixing Φ equal to 1. Metal nitrates, fuel and additives were dissolved in aqueous solution in a stainless steel beaker. The reducers-oxidizers mixture was stirred at 80 °C until a pale gel was formed. By increasing the temperature, a white dendritic powder was formed for all combustion reactions, and then fired in air for 5 h at 1000 °C. Samples were referred to with SDC-1, SDC-2 and SDC-3 abbreviations indicating the $Ce_{0.8}Sm_{0.2}O_{2-x}$ powder composition as SDC and the combustion fuel mixtures as: 1 for citric acid and ammonia; 2 for cellulose and citric acid; 3 for sucrose. The above synthesized powders were isostatically pressed at 200 MPa and treated at 1400 °C for 4 h in H_2/Ar (4vol%) for registering impedance spectroscopy analyses (see below). The final pellets had a diameter of about 7.8 mm, a thickness of about 3 mm and a density encompassed between 94 and 97% of theoretical value. The final densities were determined using the Archimedes method.

2.2. Materials characterization

X-ray diffraction (XRD) measurements were collected with a Siemens D5005 X-ray powder diffractometer equipped with a curved graphite monochromator on the diffracted beam. The observed range 25–90° 2θ was scanned with a step size of 0.02° 2θ and an integration time of 3s *per* step. Rietveld refinement of the diffraction patterns was carried out by using the GSAS package [29]. Chebyscev polynomials and Pearson VII functions were chosen for the background and for the peak profile fitting, respectively. In the structure refinement lattice constants, atomic coordinates, scale factors and full width at half maximum (FWHM) parameters were considered as variables. The estimation of the crystal size values was obtained from Scherrer equation, in agreement with the GSAS package procedure.

The X-ray photoelectron spectroscopy analyses were performed with a VG-Microtech ESCA 3000Multilab, equipped with a dual Mg/Al anode. The spectra were excited by the unmonochromatized Al Kα source (1486.6 eV) run at 14 kV and 15 mA. Since Ce(IV) could easily undergo photo-reduction, measurements were carried out with short irradiation scans in the region of Ce 3d and long irradiation times for the other elements. The Ce 3d region was recorded as soon as the sample was put under the X-Ray and afterwards all the other regions were recorded. This allowed a very low irradiation time but gave a poor signal-to-noise ratio. The analyser operated in the constant analyser energy (CAE) mode. For the individual peak energy regions, a pass energy of 20 eV set across the hemispheres was used. Survey spectra were measured at 50 eV pass energy. The sample powders were analyzed as powder, mounted on a double-sided adhesive tape. The pressure in the analysis chamber was in the range of 10^{-8} Torr during data collection. The invariance of the peak shapes and widths at the beginning and at the end of the analyses ensured absence of differential charging. Analyses of the peaks were performed with the software provided by VG, based on non-linear least squares fitting program using a weighted sum of Lorentzian and Gaussian component curves after background subtraction according to Shirley and Sherwood [30,31]. Atomic concentrations were calculated from peak intensity using the sensitivity factors provided with the software. The binding energy values are quoted with a precision of ±0.15 eV and the atomic percentage with a precision of ±10%.

Specific surface area (BET method) [32] and pore size distributions (BJH method) [33] were evaluated performing nitrogen adsorption/desorption measurements at −196 °C, using a Sorptomatic 1900Carlo Erba equipment. All the samples were pretreated under vacuum at 250 °C for 2 h prior to the measurements.
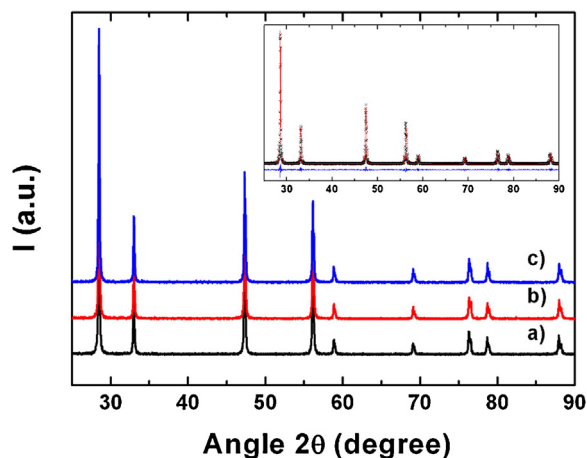
Fig. 1. XRD patterns of SDC-1 (a-black), SDC-2 (b-red) and SDC-3 (c-blue). Inset: graphical result of Rietveld refinement of SDC-1 fired at 1000 °C. Black crosses: observed data; red line: calculated data; blue line: residual.

Fig. 2. Graphical result of Rietveld refinement of SDC-1 sintered at 1400 °C under 4% H_2/Ar. Black crosses: observed data; red line: calculated data; blue line: residual.

Thermogravimetric analyses (TGA) were performed with a TGA/DSC1 STAR system Mettler Toledo. The sample (10 mg) was pretreated in N_2 (99,999% Rivoira, 30 ml min^{-1}) at 750 °C for 1 h (step 1), then it was cooled down to room temperature in air (99,999% Rivoira, 30 ml min^{-1}) purified from CO_2 and H_2O (step 2) and purged with N_2 (99,999% Rivoira, 30 ml min^{-1}) for 15 min (step 3). After that, the sample was again treated under N_2 (99,999% Rivoira, 30 ml min^{-1}) by heating (rate 5 °C/min) from room temperature up to 1000 °C (step 4). Step 1 was performed in order to remove any adsorbed water, oxygen or carbonate species; step 2 aimed to fill by oxygen all the vacancies; step 3 aimed to eliminate all the physisorbed oxygen species; step 4, during which the removal of chemisorbed oxygen species occurred, was taken into account in order to evaluate the oxygen vacancies content of the sample. The evolution of gaseous species occurring during the above four steps was monitored by on line mass quadrupole (ThermostarTM, Balzers).

Reduction properties of the oxides were studied by temperature programmed reduction (TPR) measurements in H_2/Ar (5%, 30 ml/min) in the range between room temperature and 1050 °C (heating rate 10 °C/min). Experiments were carried out with a Micromeritics Autochem 2950 instrument equipped with a thermal conductivity detector (TCD) for the evaluation of hydrogen consumption through the use of proper calibration curves. All powders (∼0.1 g) were pre-treated in O_2/He (5%, 50 ml/min) at 400 °C for 1 h and then cooled down under the same atmosphere.

Transmission Electron Microscopy measurements were obtained using a JEM-2100 (JEOL, Japan) operating at 200 kV accelerating voltage. The reduced powders were dispersed in isopropanol, and the suspension was sonicated to ensure a more homogeneous dispersion. A small drop was deposited on a 200 mesh carbon-coated copper grid, which was introduced into the TEM chamber analysis after complete solvent evaporation.

The polished surfaces of the sintered pellets were inspected by FEG-Scanning Electron Microscope (FEI Inspect F50) joined up with energy-dispersive X-ray (EDX) analysis. Polishing was done sequentially with silicon carbide powders and 15, 6, 3 and 1 μm diamond pastes, with further ultrasonic cleaning with isopropanol. The polished specimens were thermally etched at 1300 °C for 20 min to reveal the surface grain boundaries.

2.3. Electrochemical characterization

The impedance spectroscopy analyses were performed in a Hewlett-Packard 4192A LF Impedance Analyzer with a series
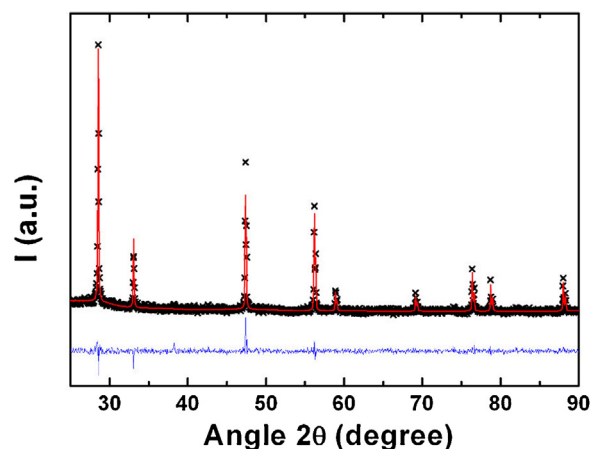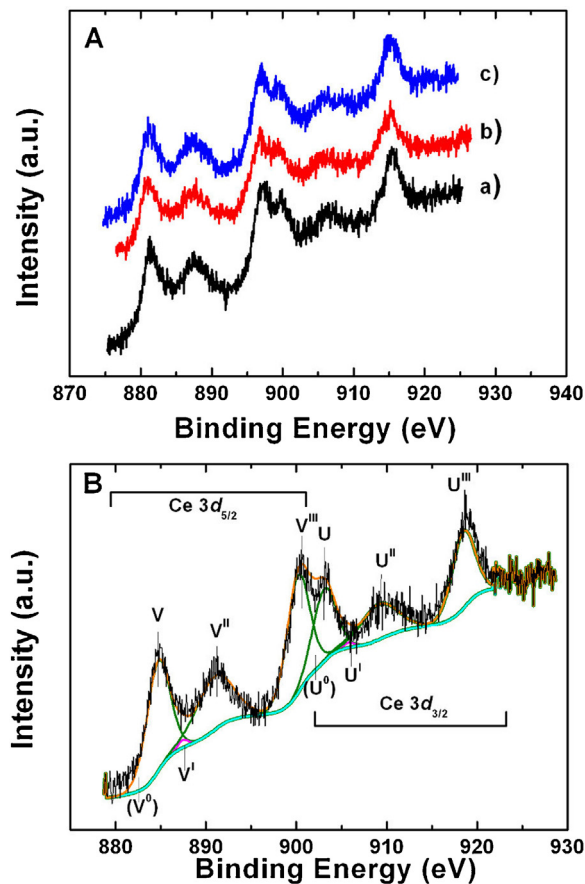

Fig. 3. High resolution Ce 3d region of SDC-1 (a-black), SDC-2 (b-red) and SDC-3 (c-blue) (panel A); SDC-1 signal (black), fitted model (orange), Ce(IV) peaks (green) and Ce(III) peaks (magenta) and background (cyan) (panel B).

900HP controller in the 5Hz–13 MHz frequency range from 190 to 350 °C. The sintered pellets, after electroding the parallel surfaces with silver paste followed by curing at 400 °C, were spring-loaded, three at a time, in an inconel-600 and alumina sample chamber, which was inserted in a programmable furnace. A special software was used for collecting and analyzing (semicircles de-convolution) the impedance data [34].

Table 1
Label, synthesis fuel and physicochemical properties of $Ce_{0.8}Sm_{0.2}O_{2-x}$ powders.

Samples	Fuel	D_{XRD} (nm)	S_{BET} (m^{2}g^{-1})	$V_p{}^a$ (cm^3 g^{-1})	Mean pore diameter (nm)	Mesopore volume (cm^3 g^{-1})
SDC-1	Citric ac.	84	15	0.07	2.5	0.039
SDC-2	Cellulose-citric ac. (2:1)	104	12	0.07	2.3	0.035
SDC-3	Sucrose	99	25	0.11	2.7	0.075

[a] V_p has been calculated at $P/P_0 = 0.99$.

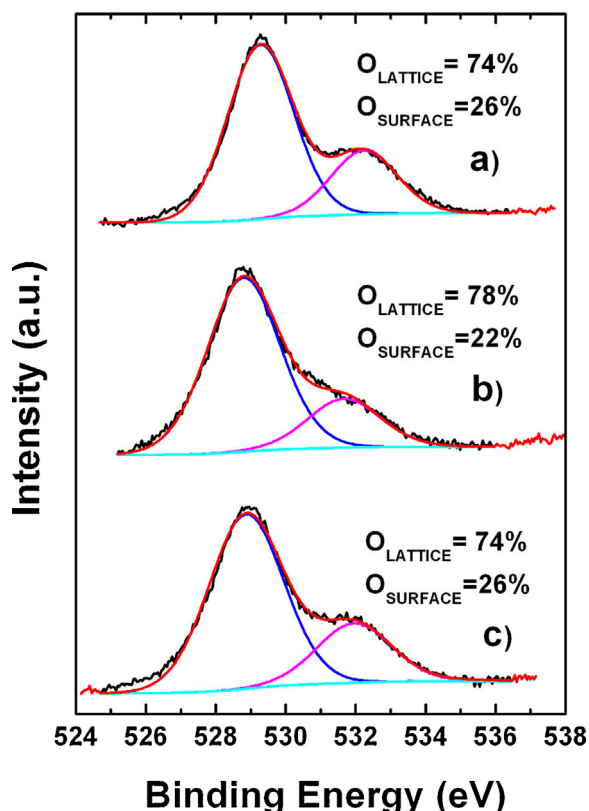**Fig. 4.** High resolution O 1s region of SDC-1 (a), SDC-2 (b) and SDC-3 (c). Signal (black), fitted model (red), $O_{LATTICE}$ peaks (blue), $O_{SURFACE}$ peaks (magenta) and background (cyan).

3. Results and discussion

Fig. 1 displays the XRD pattern collected from powders fired at 1000 °C. As confirmed by the Rietveld refinement of XRD patterns (Fig. 1-inset), all the investigated samples show a single cubic fluorite structure with cell constant $a = 5.435$ Å. The error limit is estimated to be ±0.003, whereas for Rietveld refinements the agreement factors are <10%. Consistently with our previous data, doping pure ceria with Sm(III), whose ionic radius in eightfold coordination is 1.079 Å – definitely larger than the radius (0.97 Å) of Ce(IV) [35], induces an expansion of the unit cell [5,6,36]. Actually, the ionic radius of a dopant affects the cell constant of fluorite structure according to the empirical formula proposed by Kim on the basis of Vegard's rule [37]. In particular, an expansion occurs by inserting trivalent lanthanide dopants with ionic radius higher than the critical radius (1.038 Å) determined by Kim for pure ceria [5]. As summarized in Table 1, no substantial differences in crystal size can be noticed between the investigated samples, even though SDC-1 shows slighter reduced crystal size as compared to SDC-2 and SDC-3.

For the purpose of evaluating the chemical stability of Sm-doped ceria immediately after reducing treatments at high temperature, XRD patterns were acquired after sintering procedure. Fig. 2 depicts the result of Rietveld refinement performed on the diffraction pat-

tern of SDC-1 (representative sample) powder obtained by grinding the sintered pellet. Interestingly, the cubic structure is retained with lattice parameters comparable to the values obtained after treatment in air.

Considering that H$_2$ treatment induces the formation of oxygen vacancies joined up with the charge-compensating transition of Ce(IV) to Ce(III), it could be possible that the residual concentration of Ce(III) (ionic radius 1.143 Å) counterbalances the structure contraction due to oxygen vacancies formation [5,6,38]. In addition, taking into account that a linear relationship exists between concentration and lattice parameter according to Vegard's rule, it is reasonable to assert that all samples heat treated in H$_2$ show the same Sm (III) concentration inside the grains.

XPS analysis was performed so as to evaluate the surface composition of the samples. The three samples show very similar survey patterns with the presence of peaks due to cerium, samarium and oxygen. No other contaminations, besides carbon always present as contaminant of the measure, have been seen on the surface. As what concerns cerium, its region (880–925 eV) was acquired at quick recording time (ca. 2 min) with the intention to avoid changes in the oxidation state due to the irradiation of the sample. The spectra obtained for all samples are very similar, as depicted in Fig. 3. The Ce 3d spectrum is rather complex with the presence of ten components ascribed to five pairs of spin-orbit doublets. The labeling of the peaks follows the convention of Burrough with letter V and U referring to Ce 3d$_{5/2}$ and Ce 3d$_{3/2}$, respectively. In details, the three pairs V-U, V^{II}-U^{II} and V^{III}-U^{III} arise from different electronic configuration of Ce(VI), while the two pairs V^0-U^0 and V^I-U^I correspond the two possible electron configurations of final state of Ce(III) [39]. The relative Ce(III) percentages are then calculated by the ratio between the area of the Ce(III) peaks and the total area of the Ce(III) and Ce(IV) peaks. During the fitting procedure the V^0-U^0 pair zeroed and this occurs probably due to the low amount of Ce(III). For all samples, the obtained results indicated a segregation of Ce(III) with a relative percentage of 11% ± 2%. The high error given is due to the high rate of noise in the spectra. However, the three samples show overlapping profiles indicating that the differences in the cerium oxidation state, if existing, induced by using the synthetic route are not measurable in this case with this technique. In general, it has been referred in literature that synthesis procedure influences directly the amount of Ce(III), and in the most of cases high rate of Ce(III) were achieved [38,40–42]. Thereby, with respect to other synthesis methods SCS seems to favour a low reduction rate on the surface, and this finding is encouraging for sintering under reducing atmosphere. A surface richer in Ce(IV) is advantageous for the formation of a suitable amount of oxygen vacancies and Ce(III) which are both mobile defects that promote densification under H$_2$/Ar atmosphere [5,12]. As mentioned above, the presence of Sm(III) has been testified; in details, two bands are observed at binding energies of ca.1083 attributed to Sm 3d$_{5/2}$. The Ce(IV/III)/Sm(III) atomic ratios calculated for all samples are definitely smaller compared to the theoretical ratio, 3.3 instead of 4. Actually, this variation indicates even a slight segregation of Sm on the surface. Such a small segregation, however, avoids excessive accumulation on the surface of static negative defects, Sm(III) ions, that, unlike Ce(III), hinder the coarsening between particles. O 1s spectra are shown in Fig. 4. The oxygen profile shows two mains
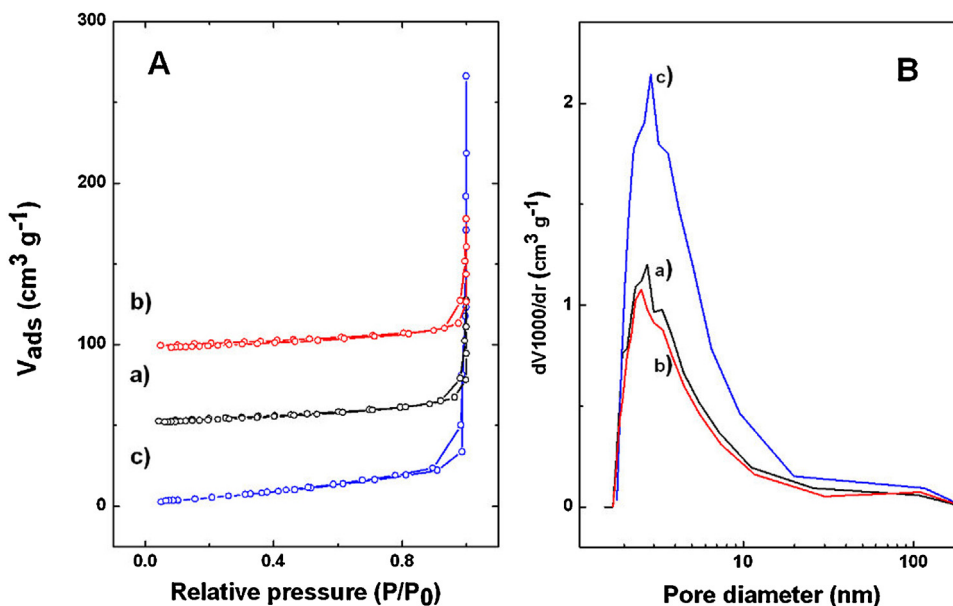
Fig. 5. N_2 adsorption/desorption isotherms for SDC-1 (a-black), SDC-2 (c-red) and SDC-3 (b-blue) (panel A) and the relative pore size distribution calculated by BJH method applied to the desorption curves (panel B).
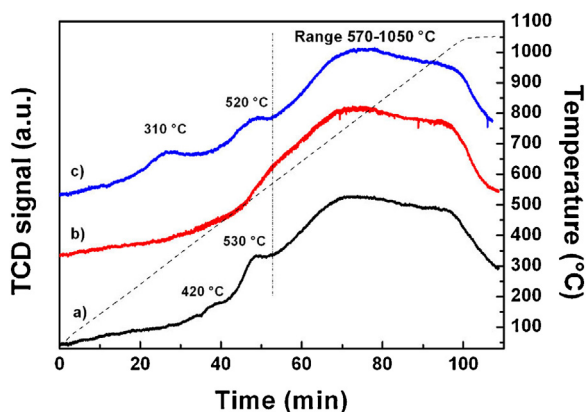

Fig. 6. H_2-TPR profiles of SDC-1 (a-black), SDC-2 (b-red) and SDC-3 (c-blue).

components at 529 and 352 eV due to lattice and hydroxyl surface groups, respectively. A comparison of the relative percentage of these two components may give some hints about differences in oxygen vacancies. A decrease of the main $O_{LATTICE}$ component with respect to the total oxygen may indeed be indicative of a higher amount of vacancies [43,44]. If we look at the oxygen profiles of our samples and at the relative percentage of the two components, given in Fig. 4, we observe very similar profiles. A slight increase of oxygen lattice with respect to the total oxygen is observed in the SDC-2 suggesting a decrease of the oxygen vacancies in the sample.

In order to assess the relative effect of synthesis fuel on morphological powder features, surface area (S_{BET}) and pore size distribution of calcined samples were estimated applying to N_2 sorption curves BET and BJH methods, respectively. Table 1 summarizes, for all specimens, the specific surface area, S_{BET}, the cumulative pore volume calculated by applying the BJH method to the desorption branch, in the range P/P_0 between 0.1 and 0.96 in order to ensure mesopores evaluation, and total pore volume, V_p, measured at $P/P_0 = 0.99$. Fig. 5 displays the N_2 adsorption/desorption isotherms and the pore size distributions associated with the $Ce_{0.8}Sm_{0.2}O_{2-x}$ powders. All the isotherms can be assigned to the type IV and are typical of relatively low

porous solids, exhibiting morphological properties comparable with values generally referred in literature for doped ceria [45]. The analysis of experimental data reveals that SDC-3, prepared with sucrose, shows a specific surface area of $25 \, m^2 g^{-1}$, higher by $\sim$70% compared to the other specimens and mesopores volume values almost double than SDC-1 and SDC-2, within the experimental error ($\pm$10%). Moreover, all three samples display a pore size distribution peak centred at $\sim$2.5. Apparently, the former effect is related to a different modulating action of sucrose molecules on the powder textures. According to combustion synthesis procedure, sucrose is able to form a gel network characterized by different levels of inter-particle agglomerates where Ce(IV) and Sm(III) ions remain trapped; therefore, during combustion event, it is reliable to consider that a cage-like structure imprinted by sucrose molecules is properly retained [20,24]. It is worth to note that this peculiar capacity of sucrose to tailor the powder morphology is maintained after heat treatment at 1000 °C. Definitely, its distinct template function acts at a level of porosity, which also plays a key role in grain growth and densification.

H_2-TPR measurements were performed up to 1050 °C with the intention to evaluate the relative reducibility of each studied sample. Fig. 6 shows TPR profiles for all samples, whereas H_2 con-

Table 2
Reduction temperatures and H_2 consumption values for $Ce_{0.8}Sm_{0.2}O_{2-x}$ powders.

Samples	T_{max} of main peak or range of temperature (°C)	H_2 consumption (ml/g) below 570 °C	Total H_2 consumption (ml/g)
SDC-1	420, 530, 570–1050	4.7	30.2
SDC-2	520–1050	1.3	29.5
SDC-3	310, 520, 570–1050	6.2	30.3

sumption values *per* gram of catalyst are summarized in Table 2 where the contribution of low-temperature peaks (below 570 °C) is pointed out. Observing TPR curves, firstly to be noted is that any given sample exhibits different reducibility features at low temperature, while by increasing the temperature the profiles enlarge and become similar to each other. A closer analysis of the experimental data reveals that SDC-2 reduction curve is dominated by a broad peak between around 570–1050 °C, with a maximum at ~790 °C, apparently ascribable to the sole Ce(IV)/Ce(III) bulk reduction. Such broad peak is common to all the specimens. Unlike the sample prepared by cellulose-citric acid, SDC-1 and SDC-3 specimens show low- and high-temperature reduction peaks, as listed in Table 2. In details, peaks at ~520–530 °C are related to surface reduction processes. Such an assignment is rather safe since it is well established that pure ceria exhibits two sharp peaks stemmed from a buffer mechanism of reduction. Generally, surface reduction process takes place under 600 °C, while subsequently at higher temperature bulk phenomena are involved [45,46]. The doping with 20 at.% of Sm remarkably influences the shape of reduction curve leading in some cases to a notable peak overlapping. For instance, in the case of gadolinium, which shows an ionic radius close to samarium one, it has been verified that the increase of dopant content leads to peak convolution [42]. Moreover, the loss of intensity for low-temperature peak relies on enhancement of oxygen mobility due to incorporation of aliovalent ions in the structure. On the other hand, low-temperature peaks can be generally recognized depending on high specific surface area [45–47]. Interestingly, SDC-3 sample manifests a second low-temperature peak, at ~310 °C, attributed to the reduction of unsaturated oxygen ions weakly bonded on the surface. This effect has been definitely explained with an enhancement of surface area, and, in particular, with a different O^{2-} availability and typology [45–47]. The absence of such very low-temperature peak for SDC-2, having the lowest BET value and the presence of a very small feature at ~420 °C for SDC-1, characterized by an intermediate value, further support the influence of specific surface area on the formation of surface oxygen vacancies. This is corroborated by XPS analysis (Fig. 4) which shows an increase of lattice oxygen to surface oxygen ratio for SDC-2 with respect to the other two samples. In the light of sintering under reducing atmosphere, SDC-3 provides a major tendency towards oxygen vacancies formation already at low temperature. This aspect is noteworthy considering that sintering in H_2 is mainly promoted at low temperature thanks to formation of defects – oxygen vacancies and Ce(III) – which enhance mass diffusion at grain boundaries and, as a consequence, grain growth.

TGA experiments were carried out in order to get further insights into the oxygen vacancies content of SDC samples. In Fig. 7A the TGA curves, in terms of weight loss percentages *vs* temperature calculated from the step 4 of the experiment, are shown. The oxygen evolution signal, at $m/z = 32$, registered by mass quadrupole during the steps 3 and 4 of TGA, is displayed for SDC-3 in Fig. 7B. For SDC-1 and SDC-3 a weight loss occurs by increasing the temperature, more pronounced in the case of SDC-3, while SDC-2 maintained fairly stable weight up to around 850 °C. According with the literature [48,49] two types of oxygen species, named as α and β, desorb from perovskites and ceria-based oxides when Temperature-Programmed Desorption (TPD) experiments are performed. The low-temperature α species usu-
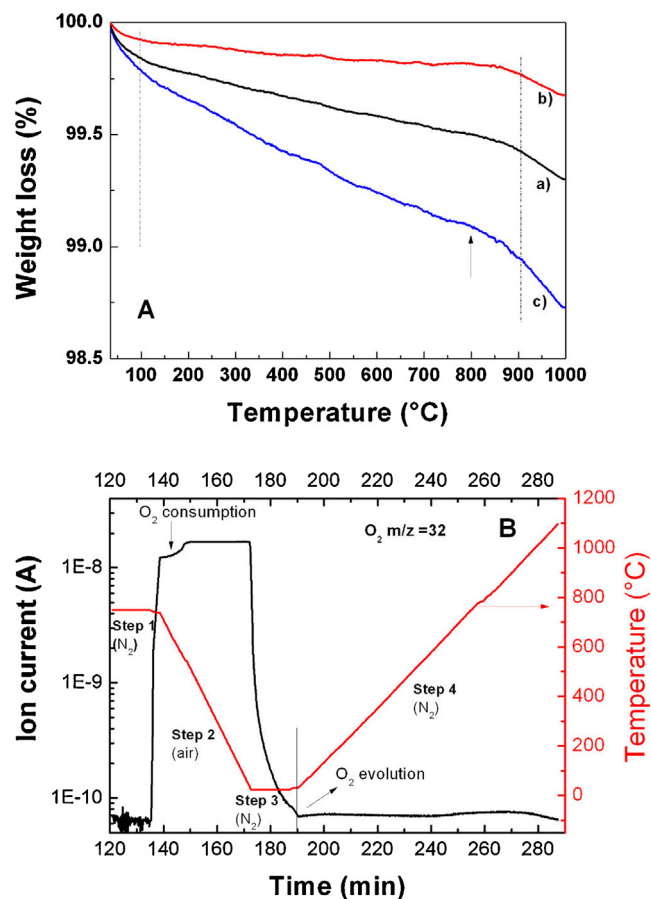

Fig. 7. TGA curves calculated from step 4 (see experimental part) for SDC-1 (a-black), SDC-2 (b-red), SDC-3 (c-blue) (panel A); Oxygen signal ($m/z = 32$) registered at the mass quadrupole for the sample SDC-3 during the TGA experiment (steps 1–4) (panel B).

ally desorb in the range ~200–600 °C, depending on the sample composition and oxygen vacancies content. Such α species correspond to weakly chemisorbed "suprafacial" species which increase with the content of oxygen vacancies in the sample. Above 600 °C desorption of the so called β type oxygen associated to "intrafacial or bulk" species usually occurs, the extent of such evolution peaks and temperature being strongly depending on the nature of reducible materials, namely perovskites, ceria or ceria-doped oxides. Looking at Fig. 7A, it is worth noting that the sample SDC-3 showed a continuous weight loss by increasing the temperature with a pronounced decreasing above 800 °C, similarly behaved the SDC-1 although much slowly. It is well-established that superoxide (O_2^-) and peroxide (O_2^{2-}) species are produced by oxygen adsorption on the surface defects of ceria [50]. According with the oxygen evolution signal recorded by QM for the SDC-3 during TGA experiment (see Fig. 7B), oxygen chemisorption takes place filling the surface oxygen vacancies of the sample (step 2), then desorption occurs under flowing N_2 and by increasing the temperature in the range 100–1000 °C (steps 3,4). Based on above discussed TPR data, TGA experiments confirm the higher oxygen vacancies content of SDC-3 with respect to SDC-1 and SDC-2 specimens. Moreover, it
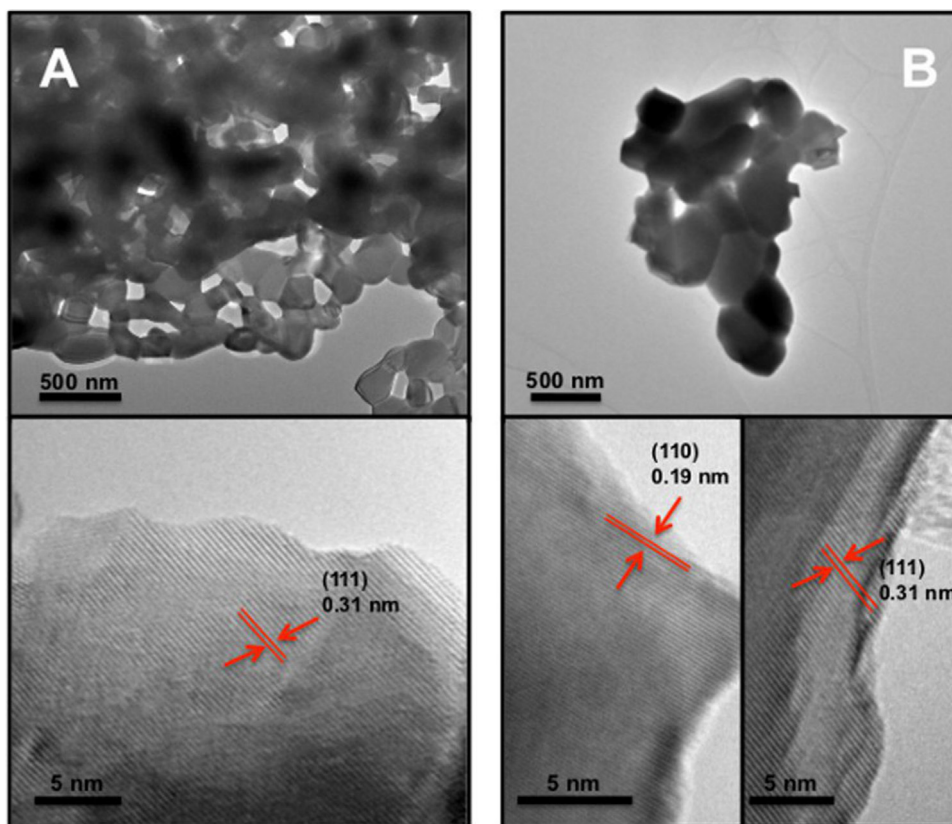
Fig. 8. Low- (up) and high- (down) resolution TEM images of SDC-2 (panel A) and SDC-3 (panel B) acquired after H_2-TPR experiments.
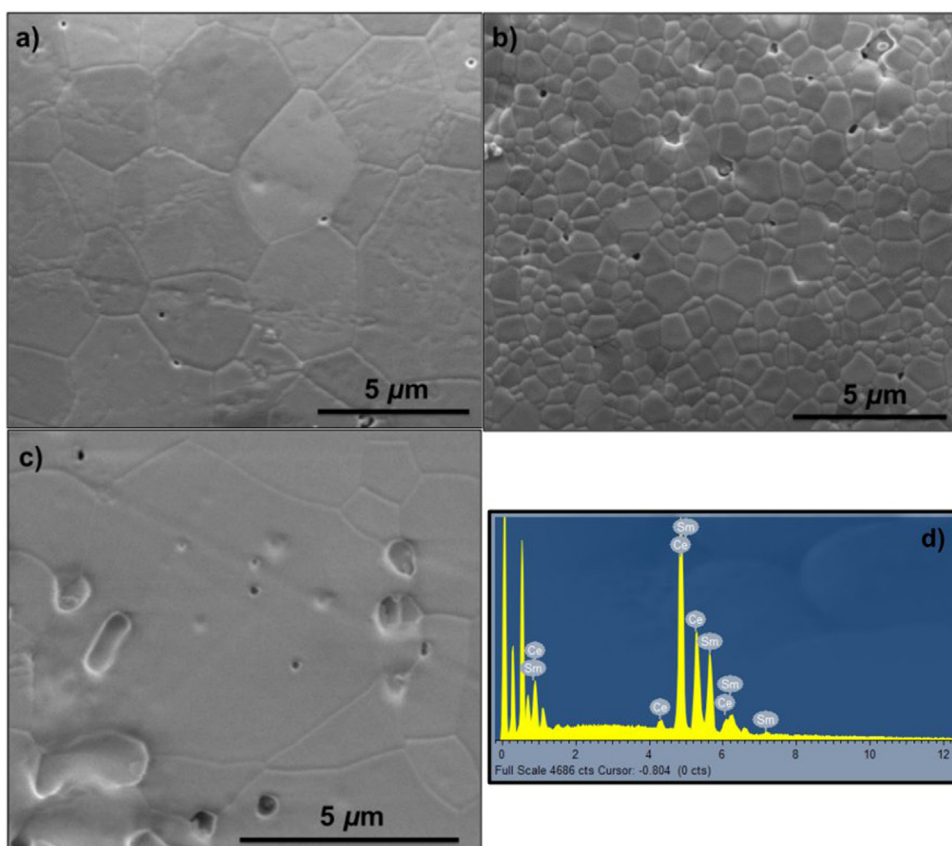

Fig. 9. Cross sections of FEG-SEM micrographs of SDC-1 (a), SDC-2 (b) and SDC-3 (c) sintered under 4% H_2-/Ar. EDX analysis collected from SDC-1 as a representative example (d).
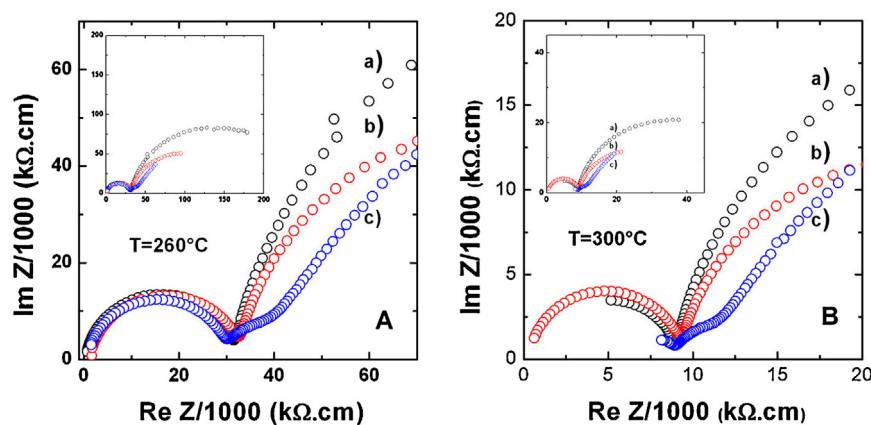
Fig. 10. Impedance spectra acquired at 260 °C (panel A) and 300 °C (panel B) in air for SDC-1 (a-black), SDC-2 (b-red) and SDC-3 (c-blue). Insets: magnification of both impedance spectra.

can be surmised that O_2 evolution peaks detected for SDC-3 in the range ∼100–900 °C of TGA curve can be ascribed to the removal of those oxygen species reduced below 570 °C in the TPR, while above 900 °C bulk oxygen removal starts to take place (see Figs. 6 and 7A).

Fig. 8 shows the typical low- and high-resolution TEM images of SDC-2 and SDC-3 samples collected after H_2-TPR experiments. The two samples were selected on the basis of both specific surface area and reducibility features. By comparing the low-resolution images, it appears that SDC-2 exhibits grains with average size of approximately 280 nm, whereas SDC-3 of *ca.* 470 nm. This finding indicates an advanced degree of coarsening for SDC-3 already at 1050 °C with respect to SDC-2, as expected on the basis of above mentioned consideration regarding reducibility features. High-resolution images reveal exposition of 1 1 1 planes (d = 0.31 nm) for both samples but, while SDC-2 shows only 1 1 1 faces, SDC-3 presents also 1 1 0 planes (d = 0.19) [43,51]. Speculating in a possible effect on densification, it is worth to note that 1 1 0 faces generally possess a more open surface array than 1 1 1 planes leading to an enhanced reactivity [51]. Consequently, it is possible to hypothesize that the presence of more reactive 1 1 0 planes for SDC-3 promotes the coarsening under hydrogen atmosphere. Actually, this hypothesis is confirmed by SEM images of sintered samples depicted in Fig. 9, from which it is evident that SDC-3 exhibits larger grains compared to the other samples. In details, the extracted average grain sizes are *ca.* 3.5, 1.3 and 6 μm for SDC-1, SDC-2 and SDC-3, respectively. Again, these results are in line with reducibility features; thus, it is reasonable to infer that the higher average grain size of SDC-3 is consistent with the different reducibility shown by this sample with respect to the other two. Nevertheless, it should be highlighted that also specific surface area, total volume and size of pores at the same time contribute to coarsening and densification. Relatively high specific surface area and total pore volume values ensure for SDC-3 the formation of larger grains compared to SDC-2 and SDC-1. Furthermore, following the considerations of Ni *et al.* concerning the effects of small pores on densification [13], it is reasonable to argue that the high amount of small pores presented by SDC-3 leads to formation of a 6 μm average size with grains up to *ca.* 9 μm. As a matter of fact, it is possible to tune the microstructure of sintered pellet with an accurate selection of synthesis fuel.

The electrical properties of the samples were studied by impedance spectroscopy in air at moderate temperatures with the intention of evaluating the capacity of synthesis fuel to tune the ionic conductivities. The impedance Nyquist plots shown in Fig. 10, registered at 260 °C and 300 °C, display two distinct contributions, which, in line with previous studies, are assigned to the bulk (high frequency contribution having $C_\infty \approx 7$ pF, from which $\varepsilon_\infty = 25$ results), the grain boundary ($C_{gb} \approx 1$ nF) and only for SDC-3 a branch
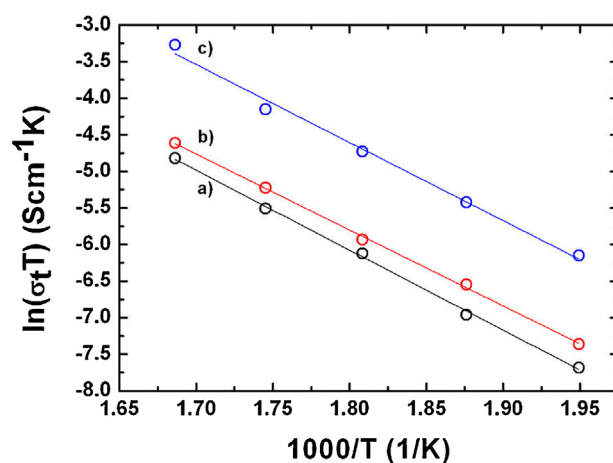

Fig. 11. Arrhenius plots for the total conductivity in air calculated by impedance data of SDC-1 (a-black), SDC-2 (b-red) and SDC-3 (c-blue).

of electrode contribution [52] . Regardless of the preparation route, all three samples manifest comparable bulk responses. Considering the same nominal composition for all samples, this finding can be explained with the same concentration of hypo-valent cations inside the grains and the same likely level of defect associations, *e.g.* $[Ln - V_o^{\bullet\bullet}]$, as well. This hypothesis is corroborated by XRD analysis that points out an unvaried lattice parameter for all the specimens. Taking into account the geometry of the samples, the extracted bulk conductivities are consistent with earlier reports concerning microcrystalline Sm-doped ceria [6,10,25]. Different grain boundary contributions emerge from Fig. 10 suggesting that both grain boundary and total conductivities are affected by synthesis route beside thermal history of the sample [6,45]. A closer look of the experimental data reveals that the sample prepared with sucrose (SDC-3) exhibits a remarkable small grain boundary semicircle with respect to the other two samples. At a first glance, this may be interpreted as a consequence of smaller volume fraction of grain boundaries in SDC-3 specimen, which facilitates the ionic transport. The average grain size is higher for this sample compared to SDC-1 and SDC-2 samples. However, grain boundary conductivity depends not only on the microstructure of the pellet, but also on solute drag effects at the grain boundaries: one factor certainly might outweigh the other on the basis of the peculiar thermal history of the sample [11]. Nevertheless, EDX analysis of SEM images (Fig. 9) revealed similar segregation of Sm(III) at grain boundaries, but this technique was not able to individuate other defects like $V_o^{\bullet\bullet}$ and Ce(III) which affect the ionic conductivity, as well. In any

case, the experimental total activation energy extrapolated from the Arrhenius's plots depicted in Fig. 11 is *ca.* 0.8 eV for all samples. In general, E_a encompasses two terms: i) migration energy for bulk diffusion, and ii) association energy due to the formation of $Ln - V_o^{\bullet\bullet}$ complexes; thus, E_a strongly depends on concentration and distribution of point defects. The activation energy results hint at a substantial similar distribution of Sm(III), Ce(III) and $V_o^{\bullet\bullet}$ between bulk and grain boundary for all samples. As a consequence, this finding corroborates the hypothesis that SDC-3 exhibits the lowest grain boundary resistance on the basis of smaller volume fraction of grain boundaries.

4. Conclusion

$Ce_{0.8}Sm_{0.2}O_{2-x}$ powders were synthesized *via* solution combustion synthesis using three different fuel mixtures. All powders show the cubic fluorite structure of pure ceria, and the structure is retained after sintering at 1400 °C under 4% H_2/Ar. The oxide prepared with sucrose displays a specific surface area and a total pore volume higher compared to the samples synthesized with citric acid and cellulose-citric acid. This effect suggests that during the synthesis sucrose is able to create a porous network system that is maintained even after heat treatment. Moreover, the high specific surface of this sample brings on a marked reducibility in H_2 at low temperature. The employed combustion fuels are able to influence the textural and redox properties of Sm-doped ceria powders, affecting as well their densification and electrochemical performance. The superior textural properties, the presence of 1 1 0 planes and the higher oxygen vacancy amount found for the sample prepared with sucrose have definitely concurred to a better densification under hydrogen and to a lower grain boundary resistance. As a matter of fact, solution combustion synthesis permits to tune the electrical features of $Ce_{0.8}Sm_{0.2}O_{2-x}$ oxides by tailoring their microstructure.

Acknowledgments

References

[1] D.J.L. Brett, A. Atkinson, N.P. Brandon, S.J. Skinner, Chem. Soc. Rev. 37 (2008) 1568–1578.
[2] A.J. Jacobson, Chem. Mater. 22 (2010) 660–674.
[3] B.C.H. Steele, Solid State Ionics 129 (2000) 95–110.
[4] J.B. Goodenough, Annu. Rev. Mater. Res. 33 (2003) 91–128.
[5] M. Mogensen, N.M. Sammes, G.A. Tompsett, Solid State Ionics 129 (2000) 63–94.
[6] F. Giannici, G. Gregori, C. Aliotta, A. Longo, J. Maier, A. Martorana, Chem. Mater. 26 (2014) 5994–6006.
[7] P. Lupetin, F. Giannici, G. Gregori, A. Martorana, J. Maier, J. Electrochem. Soc. 159 (2012) B417–B425.
[8] S. Kim, J. Maier, J. Electrochem. Soc. 149 (2002) J73–J83.
[9] A. Tschöpe, S. Kilassonia, R. Birringer, Solid State Ionics 173 (2004) 57–61.
[10] E.C.C. Souza, W.C. Chueh, W. Jung, E.N.S. Muccillo, S.M. Haile, J. Electrochem. Soc. 159 (2012) K127–K135.
[11] V. Esposito, E. Traversa, J. Am. Ceram. Soc. 91 (2008) 1037–1051.
[12] V. Esposito, D.W. Ni, Z. He, W. Zhang, A.S. Prasad, J.A. Glasscock, C. Chatzichristodoulou, S. Ramousse, A. Kaiser, Acta Mater. 61 (2013) 6290–6300.
[13] D.W. Ni, V. Esposito, S.P. Vagn Foghmoes, S. Ramousse, J. Eur. Ceram. Soc. 34 (2014) 2371–2379.
[14] M. Balaguer, C. Solís, J.M. Serra, J. Phys. Chem. C 116 (2012) 7975–7982.
[15] V. Gil, J. Tartaj, C. Moure, P. Duràn, J. Eur. Ceram. Soc. 26 (2006) 3161–3171.
[16] S.Y. Toor, Eric Croiset, ECS Trans. 68 (2015) 387–394.
[17] F. Deganello, L.F. Liotta, G. Marcì, E. Fabbri, E. Traversa, Mater. Renew. Sustainable Energy (2013) 2–8.
[18] F. Deganello, G. Marcì, G. Deganello, J. Eur. Ceram. Soc. 29 (2009) 439–450.
[19] R. Ianos, A. Taculescu, C. Pacurariu, I. Lazau, J. Am. Ceram. Soc. 95 (2012) 2236–2240.
[20] F. Li, J. Ran, M. Jaroniec, S.Z. Qiao, Nanoscale 7 (2015) 17590–17610.
[21] W. Wen, J.M. Wu, RSC Adv. 4 (2014) 58090–58100.
[22] S.L. Gonzaílez-Corteís, F.E. Imbert, Appl. Catal. A 452 (2013) 117–131.
[23] P. Bera, M.S. Hegde, RSC Adv. 5 (2015) 94949–94979.
[24] J. Ma, C. Jiang, X. Zhou, G. Meng, X. Liu, J. Alloys Compd. 455 (2008) 364–368.
[25] R.K. Lenka, T. Mahata, A.K. Tyagi, P.K. Sinha, Solid State Ionics 181 (2010) 262–267.
[26] R.K. Lenka, T. Mahata, P.K. Sinha, A.K. Tyagi, J. Alloys Compd. 466 (2008) 326–329.
[27] A. Arabaci, O. Serin, J. Mater. Eng. Perform. 24 (2015) 2730–2737.
[28] S.R. Jain, K.C. Adiga, V.R. Pai Verneker, Combust. Flame 40 (1981) 71–79.
[29] A.C. Larson, R.B. Von Dreele, GSAS General Structure Analysis System, LANSCE, MS-H805, Los Alamos National Laboratory, Los Alamos, NM 87545 USA, 1998.
[30] D.A. Shirley, Phys Rev B: Condens. Matter Mater. Phys. 5 (1972) 4709.
[31] P.M.A. Sherwood, Practical Surface Analysis, in: D. Briggs, M.P. Seah (Eds.), Wiley, New York, 1990.
[32] S. Brunauer, P.H. Emmett, E. Teller, J. Am. Chem. Soc. 60 (1938) 309–319.
[33] E.P. Barret, L.G. Joyner, P.P. Halenda, J. Am. Chem. Soc. 73 (1951) 373–380.
[34] M. Kleitz, J.H. Kennedy, Fast Ion Transport in Solids, in: P. Vashishta, J.N. Mundy, G.K. Shenoy (Eds.), Elsevier North Holland, The Netherlands, 1979, p. 185.
[35] R.D. Shannon, C.T. Prewitt, Acta Crystallogr. B 25 (1969) 925–946.
[36] E.Y. Pikalova, A.A. Murashkina, V.I. Maragou, A.K. Demin, V.N. Strekalovsky, P.E. Tsiakaras, Int. J. Hydrogen Energy 36 (2011) 6175–6183.
[37] D.J. Kim, J. Am. Ceram. Soc. 72 (1989) 1415–1421.
[38] N. Sutradhar, A. Sinhamahapatra, S. Pahari, M. Jayachandran, B. Subramanian, H.C. Bajaj, A.B. Panda, J. Phys. Chem. C 115 (2011) 7628–7637.
[39] P. Burroughs, A. Hamnett, A. Orchard, G. Thornton, J. Chem. Soc. Dalton Trans. (1976) 1686.
[40] S.A. Acharya, V.M. Gaikwad, S.W. D'Souza, S.R. Barman, Solid State Ionics 260 (2014) 21–29.
[41] S. Liang, E. Broitman, Y. Wang, A. Cao, G. Veser, J. Mater. Sci. 46 (2011) 2928–2937.
[42] J. Marrero-Jerez, S. Larrondo, E. Rodríguez-Castellón, P. Núñeza, Ceram. Int. 40 (2014) 6807–6814.
[43] H. Tan, J. Wang, S. Yu, K. Zhou, Environ. Sci. Technol. 49 (2015) 8675–8682.
[44] M. Konsolakis, M. Sgourakis, S.A.C. Carabineiro, Appl. Surf. Sci. 341 (2015) 48–54.
[45] A. Pappacena, P. Porreca, M. Boaro, C. de Leitenburg, A. Trovarelli, Int. J. Hydrogen Energy 37 (2012) 1698–1709.
[46] Y. Wang, S. Liang, A. Cao, R.L. Thompson, G. Veser, Appl. Catal. B 99 (2010) 89–95.
[47] G.R. Rao, Bull. Mater. Sci. 22 (1999) 89–94.
[48] D. Fino, N. Russo, G. Saracco, V. Specchia, J. Catal. 217 (2003) 367–375.
[49] L.F. Liotta, M. Ousmane, G. Di Carlo, G. Pantaleo, G. Marcì, L. Retailleau, A. Giroir-Fendler, Appl. Catal. A 347 (2008) 81–88.
[50] C. Binet, M. Daturi, J.C. Lavalley, Catal. Today 50 (1999) 207–225.
[51] X. Liu, K. Zhou, L. Wang, B. Wang, Y. Li, J. Am. Chem. Soc. 131 (2009) 3140–3141.
[52] J.G. Fletcher, A.R. West, J.T.S. Irvine, J. Electrochem. Soc. 142 (8) (1995) 2650–2654.